

UC Berkeley

UC Berkeley Previously Published Works

Title

Synthesis and Polymorph Manipulation of FeSe₂ Monolayers

Permalink

<https://escholarship.org/uc/item/96k1h77s>

Journal

Nano Letters, 24(28)

ISSN

1530-6984

Authors

He, Zehao

Poudel, Shiva Prasad

Stolz, Samuel

et al.

Publication Date

2024-07-17

DOI

10.1021/acs.nanolett.4c01286

Copyright Information

This work is made available under the terms of a Creative Commons Attribution-NonCommercial-NoDerivatives License, available at

<https://creativecommons.org/licenses/by-nc-nd/4.0/>

Peer reviewed

Synthesis and polymorph manipulation of FeSe₂ monolayers

Zehao He^{1,2,3*}, Shiva Prasad Poudel^{4*}, Samuel Stolz^{1*}, Tiancong Zhu^{1,2*}, Tianye Wang^{1,2},

Antonio Rossi⁵, Feng Wang^{1,2,6}, Sung-Kwan Mo⁷, Alexander Weber-Bargioni⁵, Zi Qiang

Qiu^{1,2}, Salvador Barraza-Lopez⁴, and Michael F. Crommie^{1,2,6}

¹*Department of Physics, University of California, Berkeley, CA 94720, USA.*

²*Materials Sciences Division, Lawrence Berkeley National Laboratory, Berkeley, CA 94720, USA.*

³*Department of Material Science and Engineering, University of California, Berkeley, CA 94720, USA.*

⁴*Department of Physics, University of Arkansas, Fayetteville, Arkansas 72701, USA and MonArk NSF Quantum Foundry, University of Arkansas, Fayetteville, Arkansas 72701, USA.*

⁵*The Molecular Foundry, Lawrence Berkeley National Laboratory, Berkeley, California 94720, USA.*

⁶*Kavli Energy NanoScience Institute at the University of California, Berkeley and the Lawrence Berkeley National Laboratory, Berkeley, CA 94720, USA.*

⁷*Advanced Light Source, Lawrence Berkeley National Laboratory, Berkeley, CA 94720, USA.*

Corresponding author e-mail address: crommie@berkeley.edu

1
2
3 **Abstract**
4

5 Polymorph engineering involves the manipulation of material properties through a controlled
6 structural modification and is a candidate technique for creating unique 2D transition metal
7 dichalcogenide (TMDC) nanodevices. Despite its promise, polymorph engineering of *magnetic*
8 TMDC monolayers has not yet been demonstrated. Here we grow FeSe₂ monolayers via
9 molecular beam epitaxy (MBE) and find that they have great promise for magnetic polymorph
10 engineering. Using scanning tunneling microscopy (STM) and spectroscopy (STS) we find that
11 FeSe₂ monolayers predominantly display a 1T' structural polymorph at 5 K. Application of
12 voltage pulses from an STM tip causes a local, reversible transition from the 1T' phase to the
13 1T phase. Density functional theory (DFT) calculations suggest that this single-layer structural
14 phase transition is accompanied by a magnetic transition from an antiferromagnetic to a
15 ferromagnetic configuration. Those results open new possibilities for creating functional
16 magnetic devices with TMDC monolayers via polymorph engineering.
17
18
19
20
21
22
23
24
25
26
27
28
29
30
31
32
33
34
35

36 **Keywords**
37

38 Polymorphism, magnetism, two-dimensional materials, scanning tunneling microscopy, phase
39 transitions, density-functional theory
40
41
42
43
44
45
46
47
48
49
50
51
52
53
54
55
56
57
58
59
60

1
2
3 TMDC monolayers have demonstrated great potential for next-generation electronic,
4 magnetic, and optical applications.¹ These atomically-thin materials host a variety of novel
5 phenomena including non-trivial topology,²⁻⁴ superconductivity,^{5,6} charge density waves,^{5,7-9}
6 magnetism,^{10,11} and Mott insulating phases^{6,12,13}, most of which are highly tunable through
7 electrostatic gating and strain.¹⁴⁻¹⁸ The coexistence of different crystal structures having the
8 same stoichiometry in TMDC monolayers provides unique opportunities for TMDC
9 polymorph engineering. The three main polymorphs for TMDC monolayers are the trigonal
10 prismatic (1H), the octahedral (1T), and the distorted octahedral (1T') lattices, each of which
11 exhibits very different physical properties. Structural manipulation between TMDC monolayer
12 polymorphs has been used to induce topological transitions between the 1T' and 1H phases in
13 WSe₂ and MoTe₂,^{19,20} as well as metal-insulator transitions between the 1H and 1T phases of
14 TaSe₂, TaS₂, and NbSe₂.²¹⁻²³ Polymorph engineering of TMDC monolayers has been achieved
15 through temperature,²⁴ strain,¹⁴ charge doping,^{15,16} laser irradiation,²⁵ and by applying local
16 electric fields,^{21-23,26} thus expanding the toolbox for creating functional devices based on
17 TMDC monolayers. Despite rapid progress in experimentally controlling polymorphism in
18 TMDC monolayers, however, the manipulation of magnetism in these materials through
19 polymorph engineering is still in its infancy, mainly due to a lack of suitable material platforms.
20
21
22
23
24
25
26
27
28
29
30
31
32
33
34
35
36
37
38
39
40
41
42

43 Here we demonstrate that monolayer FeSe₂ is a promising candidate for magnetic
44 polymorph engineering through a combined experimental and theoretical investigation. The
45 FeSe₂ monolayers used in this study were grown *via* molecular beam epitaxy (MBE). STM
46 investigation reveals that our FeSe₂ monolayers occur mainly in a stripe phase that we identify
47 as the 1T'-polymorph. We find that FeSe₂ monolayers can be locally converted into a
48 hexagonal phase that we identify as the 1T-FeSe₂ polymorph upon application of voltage pulses
49 from the STM tip. This phase transition can be reversed by heating the sample above 50 K,
50 thus establishing the 1T'-polymorph as the ground state structure. DFT+U calculations confirm
51
52
53
54
55
56
57
58
59
60

1
2
3 the assignment of 1T' and 1T polymorphs to the stripe and hexagonal phases and corroborate
4 that 1T'-FeSe₂ is the most stable polymorph and that it has a low energy barrier for structural
5 phase transitions. Our calculations further suggest the existence of antiferromagnetic order in
6 monolayer 1T'-FeSe₂ and ferromagnetic order in the monolayer 1T-FeSe₂ phase over a large
7 range of values for the parameter U.
8
9

10
11
12
13
14
15 FeSe₂ monolayers were grown on highly oriented pyrolytic graphite (HOPG) using
16 MBE under a Se-rich environment (see methods for growth details). The growth was monitored
17 using reflection high-energy electron diffraction (RHEED) as shown in Fig. 1a. We observe
18 concurrent growth of FeSe and FeSe₂ monolayers. During growth at 800 K the RHEED
19 intensity from FeSe₂ monolayer (red lines in Fig. 1a) is stronger than monolayer FeSe intensity
20 (green lines in Fig. 1a). Upon cool-down to 300 K the relative RHEED intensity of monolayer
21 FeSe increases, indicating that monolayer FeSe₂ is a metastable phase.
22
23
24
25
26
27
28
29
30
31

32 Low temperature (5 K) STM and STS measurements were performed to gain insight
33 into the structural and electronic properties of monolayer FeSe₂. The large-scale STM image
34 shown in Fig. 1b depicts monolayer FeSe₂ islands on HOPG that have a step height of about
35 8.2 ± 0.2 Å. The high-resolution STM images and STS data shown in Figs. 1c - f enable us to
36 differentiate the structure and density of states of monolayer FeSe *versus* monolayer FeSe₂.
37 Monolayer FeSe (Fig. 1c) is observed to have a square unit cell with lattice constant $3.8 \text{ Å} \pm$
38 0.1 Å , as seen previously²⁷. Our STS spectra obtained from monolayer FeSe (Fig. 1f, green
39 curve) is also in agreement with previous STS measurements²⁷. All non-FeSe monolayer
40 islands are identified as FeSe₂ and are observed to have two different polymorphs. The majority
41 of FeSe₂ monolayer islands show a stripe phase (Fig. 1d), accounting for more than 90% of
42 total FeSe₂ island area. An atomically resolved image of the stripe phase reveals a rectangular
43 unit cell with lattice constants $3.9 \text{ Å} \pm 0.1 \text{ Å}$, $6.7 \text{ Å} \pm 0.1 \text{ Å}$ (Fig. 1d, bottom panel). The atomic
44 structure and symmetry of the stripe phase is similar to previous observations of 1T'-WTe₂⁴
45
46
47
48
49
50
51
52
53
54
55
56
57
58
59
60

1
2
3 (although a slight period-doubling in the long direction can be seen for FeSe₂ (see
4 Supplementary Fig. 1)). The remaining fraction of the FeSe₂ monolayer islands exhibit a
5 hexagonal phase with lattice constant $3.8 \text{ \AA} \pm 0.1 \text{ \AA}$ (Fig. 1e) that is consistent with either the
6 1T or the 1H TMDC polymorphs. STS measurements shown in the inset to Fig. 1f reveal that
7 both phases of monolayer FeSe₂ exhibit a non-vanishing dI/dV signal near the Fermi level, thus
8 indicating metallic behavior.
9

10
11
12
13
14
15
16
17
18 Fig. 2 shows the process by which the stripe phase of monolayer FeSe₂ can be locally
19 converted into the hexagonal phase by applying a voltage pulse from the STM tip. Fig. 2a
20 shows an FeSe₂ island before tip pulsing where most of the island is in the stripe phase (see
21 dashed line phase boundary). To induce a local phase change, the STM tip was positioned at
22 the location indicated by the white cross in Fig. 2b and a voltage pulse of + 3.4 V was applied
23 for 100 ms with the STM feedback loop open ($V_B = -1 \text{ V}$, $I_T = 10 \text{ pA}$ for the tunnel set point).
24 After the pulse the region near the tip-pulse position is seen to convert from the stripe phase to
25 the hexagonal phase (see lower dashed line boundary). The close-up image in the inset to Fig.
26 2b shows the hexagonal symmetry of the converted region (this region has an area similar to
27 the altered regions observed in other STM-driven phase transitions^{21,28,29}). The rest of the island
28 was converted from the stripe phase to the hexagonal phase by scanning the entire island with
29 a bias voltage $V_B = + 3.5 \text{ V}$ ($I_T = 10 \text{ pA}$) (Fig. 2c). Once converted to the hexagonal phase, the
30 island could not be changed back to the stripe phase by pulsing despite applying numerous
31 voltage pulses in the range $- 5 \text{ V} < V_{pulse} < + 5 \text{ V}$.
32
33
34
35
36
37
38
39
40
41
42
43
44
45
46
47
48
49

50
51 To better characterize the phase conversion process, we systematically determined the
52 threshold pulse voltage required to convert different stripe-phase islands to the hexagonal
53 phase. For each island a low voltage pulse of + 2 V was first applied (using the initial tunnel
54 set point $V_B = -1 \text{ V}$, $I_T = 10 \text{ pA}$) and then incrementally higher pulses were applied up to a
55 maximum of + 5 V (using the same initial set point) *until* a tip-induced structural phase
56
57
58
59
60

1
2
3 transition occurred. A histogram of the minimum voltage pulse required to cause local phase
4 conversion at $T = 5$ K for different monolayer islands is plotted in Fig. 2d. Stripe phase islands
5 that did not convert to the hexagonal phase after applying voltage pulses up to + 5 V are denoted
6 “non-convertible” (NC). The phase conversion process is observed to be polarity-dependent,
7 as no islands could be converted with negative pulses up to a magnitude of -4 V. At $T = 5$ K
8 98% of all monolayer islands in the stripe phase could be converted to the hexagonal phase
9 using positive pulses (Fig. 2d) with the average threshold voltage being $\langle V_{th} \rangle = 3.3$ V. No
10 clear trend is seen regarding the area of the converted FeSe₂ region and the magnitude of the
11 applied voltage pulse (see Supplementary Fig. 2). Possible mechanisms that might explain the
12 1T'-to-1T phase transition observed here include the effect of the tip-induced electric field on
13 local electronic dipole moments^{21,29}, as well as the effect of electronic doping on the total
14 energy of the 2D film^{15,20}.

15
16
17
18
19
20
21
22
23
24
25
26
27
28
29
30
31 The ease with which the stripe-to-hexagonal phase transition of FeSe₂ monolayers can
32 be induced suggests a relatively low energy barrier between the stripe and hexagonal
33 polymorphs. This implies that thermally-induced island structural transitions might be able to
34 compete with tip-induced transitions at elevated temperatures. To test this hypothesis and gain
35 insight into the magnitude of the relevant energy barrier, we performed additional experiments
36 at higher temperatures using the switching protocol described above. Fig. 3a shows the tip-
37 induced switching histogram for an ensemble of islands held at $T = 20$ K. The observed
38 switching characteristics are very similar to those occurring at $T = 5$ K: all 23 islands were
39 switched with $\langle V_{th} \rangle = 3.1$ V. At higher temperatures, however, the switching behavior of the
40 islands gradually changes. For example, Fig. 3b shows that at $T = 40$ K the threshold voltage
41 raises to $\langle V_{th} \rangle = 3.5$ V and 11% of the islands are non-convertible. At $T = 50$ K the threshold
42 voltage increases to $\langle V_{th} \rangle = 3.9$ V and 27% of the islands cannot switch (Fig. 3c). At $T = 60$
43 K the threshold voltage increases further to $\langle V_{th} \rangle = 4.4$ V, while the non-switching fraction
44
45
46
47
48
49
50
51
52
53
54
55
56
57
58
59
60

1
2
3 jumps to 54% (Fig. 3d). The temperature-induced trend is seen in Fig. 3e which shows the non-
4 switching fraction of islands as a function of temperature.
5
6

7
8 In addition to the apparent increased difficulty of switching with increased temperature,
9 we also observe islands switching *back* to the stripe phase at higher temperatures. For example,
10 at $T = 20$ K no islands return to the stripe phase for waiting times on the order of 1 minute
11 while at $T = 50$ K we observe 25% of the islands switching back to the stripe phase after a 1
12 minute waiting period. The increased difficulty of the $1T'$ -to- $1T$ phase transition with increased
13 temperature is likely influenced by the increased rate of back conversions. This is consistent
14 with the fact that the striped $1T'$ phase of monolayer FeSe_2 is the thermodynamically stable
15 phase.
16
17
18
19
20
21
22
23
24
25
26

27 The temperature dependence of the switching behavior can be visualized for a single
28 monolayer island as shown in Figs. 3f – i. Fig. 3f shows the entire island in the stripe phase at
29 $T = 50$ K before switching (the dashed black line shows a grain boundary between two rotated
30 $1T'$ domains (see SI section 3 for additional discussion of domain boundaries)). Fig. 3g shows
31 the island after being pulsed at the marked location, causing the lower right quadrant to switch
32 to the hexagonal phase ($T = 50$ K). The sample was then warmed to $T = 60$ K over a period of
33 $\Delta t \sim 1$ hour, whereupon the same island was reimaged. As shown in Fig. 3h, heating causes
34 the island to switch back to the stripe phase with a grain boundary bisecting the island between
35 two rotated $1T'$ domains (similar phase reversal also occurs for fully converted $1T$ islands as
36 shown in SI section 4). This island could not be switched to the hexagonal phase via tip pulsing
37 at $T = 60$ K, but the $1T'$ - $1T'$ rotational grain boundary did shift as a result of pulsing (Fig. 3i)
38 (similar tip-pulse-induced movement of $1T'$ - $1T'$ grain boundaries has been seen in TMDC
39 monolayers previously²⁶).
40
41
42
43
44
45
46
47
48
49
50
51
52
53
54
55
56
57
58
59
60

1
2
3 To gain further insight into the properties of monolayer FeSe₂ we performed DFT
4 calculations using the DFT+U method with U values ranging from 0 to 6 eV for the Fe *d*-
5 orbital. As shown in Fig. 4a, our relaxed DFT structures systematically underestimate the
6 lattice constants of the 1T' and 1T FeSe₂ polymorphs by about 9% compared to the STM data
7 (the energetically unfavorable 1H polymorph has a lattice constant that is more than 18%
8 smaller than the experimental hexagonal lattice constant). Slight underestimation of lattice
9 constants is common for DFT-based methods.³⁰⁻³³ Our DFT calculations provide useful insight
10 into the energetics of the different FeSe₂ polymorphs, including their magnetic configurations.
11 As shown in Fig. 4b, the 1T'-FeSe₂ monolayer is the energetically favorable polymorph for U
12 ≤ 4 eV (more than 160 meV per formula unit (f.u.) lower in energy than 1H-FeSe₂) but is only
13 ~ 5 meV per formula unit (f.u.) more stable than monolayer 1T-FeSe₂ for U = 4 eV. This leads
14 to an energy difference of ~ 50 K between the 1T-FeSe₂ and 1T'-FeSe₂ phases, in reasonable
15 agreement with the experimental results and supporting our choice of U = 4 eV.
16
17
18
19
20
21
22
23
24
25
26
27
28
29
30
31
32

33 Our DFT calculations provide insight into the magnetic ground states of the different
34 polymorphs of monolayer FeSe₂. Fig. 4c shows that the 1T' rectangular AFM phase has the
35 lowest energy of all the polymorph phases while the 1T FM phase is the nearest adjacent phase
36 with an energy just 5 meV/f.u. higher (theoretically predicted magnetic orderings were seen to
37 remain constant for electron and hole doping levels up to 10¹³/cm²). No experimental signatures
38 of inelastically-induced transitions between different theoretically predicted magnetic phases
39 were observed for our FeSe₂ samples.
40
41
42
43
44
45
46
47
48
49

50 The magnetic moments of the 1T' rectangular AFM phase are predicted to have a
51 magnitude of 3.59 μ_B per Fe atom and 0.09 μ_B per Se atom. The nearby 1T FM phase is
52 predicted to have magnetic moments of 3.69 μ_B per Fe atom and 0.116 μ_B per Se atom (spin-
53 polarized band structures for these magnetic configurations can be seen in Fig. 4e and are
54 compared to experimental dI/dV spectra in Supplementary Fig. 6). The ferromagnetic 1T-FeSe₂
55
56
57
58
59
60

1
2
3 monolayer adopts an in-plane magnetic configuration with a magnetic anisotropy barrier of 1.1
4 meV per formula unit (Fig. 4d), consistent with an observed phase transition in
5
6 magnetoresistance measured previously for multilayer 1T-FeSe₂ nanocrystals.³⁴
7
8
9

10
11 The calculated magnetic states of both 1T-FeSe₂ and 1T'-FeSe₂ are consistent with each
12
13 Fe atom transferring four electrons to surrounding Se atoms, thus changing the Fe electron shell
14 structure from $4s^23d^6$ to $4s^03d^4$. The four remaining *d*-electrons are expected to result in $4 \mu_B$
15 per Fe atom according to Hund's rule, which is reasonably consistent with our calculated
16
17 magnetic moments. Because Fe atoms in FeSe₂ are next-nearest neighbors, the magnetic
18 exchange interaction is likely dominated by super-exchange coupling through Se atoms, whose
19 sign and magnitude can strongly depend on bond length and bond angles. This is the probable
20 cause of the different magnetic ground states between monolayer 1T-FeSe₂ and monolayer 1T'-
21 FeSe₂.
22
23
24
25
26
27
28
29
30
31

32 In conclusion, we have experimentally demonstrated growth of the 1T' polymorph of
33 monolayer FeSe₂, as well as reversible manipulation between monolayer FeSe₂ 1T'- and 1T-
34 polymorphs. The 1T'-FeSe₂ to 1T-FeSe₂ transition is realized electrically by applying a voltage
35 pulse with the STM tip, while the 1T-FeSe₂ to 1T'-FeSe₂ transition is produced thermally. DFT
36 simulations suggest that this structural phase transition is accompanied by a change from
37 antiferromagnetic ordering in monolayer 1T'-FeSe₂ to ferromagnetic ordering in monolayer
38 1T-FeSe₂. The predicted difference in magnetic ordering between the 1T and 1T' phases
39 combined with the experimentally observed reversible structural phase transition suggests that
40 the magnetic ground state of FeSe₂ monolayers may be locally manipulated through their
41 structural polymorph. FeSe₂ monolayers thus potentially provide a new platform for the
42 investigation and manipulation of structural and magnetic phase transitions in the atomically
43 thin limit.
44
45
46
47
48
49
50
51
52
53
54
55
56
57
58
59
60

Methods

MBE growth

Monolayer FeSe₂ samples were grown on highly-oriented pyrolytic graphite (HOPG) or on bilayer graphene on SiC(0001) substrates using molecular beam epitaxy. Before growth the substrates were cleaned by annealing them at 900 K overnight under ultra-high vacuum conditions with a pressure better than 2×10^{-10} mbar. Iron (Purity: 99.995%, SPIE) and selenium (Purity: 99.999%, Alfa Aesar) were then sublimated from an e-beam evaporator (flux: 0.08 Å/min) and a home-built Knudsen cell (flux: 8 Å/min) respectively until the desired surface coverage was achieved while holding the sample at 800 K.

STM measurements

Clean transfer of the sample from the MBE chamber to the STM chamber was achieved by capping the sample with 20 nm of amorphous Se to prevent degradation in air. Before STM measurement the samples were annealed in UHV at ~ 200 °C for 1 h to remove the Se capping layer and then transferred *in-situ* to the low temperature ($T = 5$ K) STM stage. Some samples were directly transferred from the MBE chamber to the STM chamber through a UHV suitcase to confirm the quality of the Se-capped samples.

STM measurements were performed in a low-temperature CreaTec UHV STM operated at a pressure below 2×10^{-10} mbar ($T = 5$ K for all STM measurements except where otherwise specified). Electrochemically etched tungsten tips were calibrated on a Cu(111) surface before performing other STM measurements. STS measurements were performed using standard lock-in techniques (frequency = 401 Hz). The STM tip was grounded during these measurements and bias voltages refer to the sample voltage.

To determine the lattice constants of epitaxial FeSe₂ monolayers we first calibrated our STM by obtaining atomic resolution of the underlying HOPG or graphene substrate. The STM

1
2
3 set point before applying voltage pulses for monolayer phase switching was typically $V_B = -1$
4
5 V, $I_T = 10$ pA. Voltage pulses of + 2 V were first applied and then increased by + 0.1 V until
6
7 the stripe-to-hexagonal phase transition was observed via STM topography scans.
8
9

10 Computational methods

11
12
13 Electronic structure calculations were performed using density-functional theory as
14 implemented in the VASP package³⁵. PAW³⁶ pseudopotentials were used to describe the ionic
15 potential of all atoms. We employed exchange-correlation functionals with self-consistent van
16 der Waals corrections³⁷ using the optPBE-vdW functional.³⁸⁻⁴⁰ A 30 x 15 x 1 k-point grid and
17
18 cutoff energy of 500 eV were employed. Energy and force convergence criteria were set to
19
20 10^{-10} eV and 10^{-6} eV/Å, respectively. The out-of-plane lattice vector was set to 30 Å. A U-
21
22 parameter was added to constrain the spatial extent of the Fe *d*-orbitals, which are often too
23
24 extended in standard DFT. This approach also helps to provide more accurate magnetic
25
26 exchange couplings. We applied DFT+U corrections^{41,42} using the method by Dudarev *et al.*⁴³.
27
28
29
30
31
32
33
34

35 **Acknowledgements**

36
37
38 This research was supported by the Director, Office of Science, Office of Basic Energy
39 Sciences, Materials Sciences and Engineering Division of the US Department of Energy, under
40 contract number DE-AC02-05CH11231 within the van der Waals Heterostructures program
41 (KCWF16) (STM/STS measurements). Support was also provided by the Center for Novel
42 Pathways to Quantum Coherence in Materials, an Energy Frontier Research Center funded by
43 the US Department of Energy, Office of Science, Basic Energy Sciences (MBE growth and
44 characterization) and the National Science Foundation under grant DMR-2221750 (phase
45 switching analysis). S.S. acknowledges Fellowship support by the Swiss National Science
46 Foundation under project no.195133. S.P.P. and S.B.L. were supported by the National Science
47 Foundation Q-AMASE-i program under grant DMR-1906383 (magnetic structure
48
49
50
51
52
53
54
55
56
57
58
59
60

1
2
3 simulations). DFT calculations were performed at the Pinnacle Supercomputer, funded by NSF
4
5 under award OAC-2346752.
6
7

8 **Data availability** 9

10 The data presented in the paper is available under request.
11
12

13 **Ethics declaration** 14

15 The authors declare no competing interests.
16
17
18
19

20 **Supporting Information** 21

22 The supporting information contains Section 1: Atomic structure of monolayer FeSe₂
23 stripe phase; Section 2: Statistics for converted area versus magnitude of voltage pulses;
24
25 Section 3: Additional experimental data on domain walls; Section 4: Phase reversal for a fully
26
27 converted 1T island and Section 5: Experimental dI/dV spectra and calculated density of states
28
29 (DOS).
30
31
32
33
34
35
36
37
38
39
40
41
42
43
44
45
46
47
48
49
50
51
52
53
54
55
56
57
58
59
60

References

- (1) Manzeli, S.; Ovchinnikov, D.; Pasquier, D.; Yazyev, O. V.; Kis, A. 2D Transition Metal Dichalcogenides. *Nat. Rev. Mater.* **2017**, *2* (8), 1–15.
<https://doi.org/10.1038/natrevmats.2017.33>.
- (2) Fei, Z.; Palomaki, T.; Wu, S.; Zhao, W.; Cai, X.; Sun, B.; Nguyen, P.; Finney, J.; Xu, X.; Cobden, D. H. Edge Conduction in Monolayer WTe_2 . *Nat. Phys.* **2017**, *13* (7), 677–682. <https://doi.org/10.1038/nphys4091>.
- (3) Wu, S.; Fatemi, V.; Gibson, Q. D.; Watanabe, K.; Taniguchi, T.; Cava, R. J.; Jarillo-Herrero, P. Observation of the Quantum Spin Hall Effect up to 100 Kelvin in a Monolayer Crystal. *Science* **2018**, *359* (6371), 76–79.
<https://doi.org/10.1126/science.aan6003>.
- (4) Tang, S.; Zhang, C.; Wong, D.; Pedramrazi, Z.; Tsai, H.-Z.; Jia, C.; Moritz, B.; Claassen, M.; Ryu, H.; Kahn, S.; Jiang, J.; Yan, H.; Hashimoto, M.; Lu, D.; Moore, R. G.; Hwang, C.-C.; Hwang, C.; Hussain, Z.; Chen, Y.; Ugeda, M. M.; Liu, Z.; Xie, X.; Devereaux, T. P.; Crommie, M. F.; Mo, S.-K.; Shen, Z.-X. Quantum Spin Hall State in Monolayer $1\text{T}'\text{-WTe}_2$. *Nat. Phys.* **2017**, *13* (7), 683–687.
<https://doi.org/10.1038/nphys4174>.
- (5) Ugeda, M. M.; Bradley, A. J.; Zhang, Y.; Onishi, S.; Chen, Y.; Ruan, W.; Ojeda-Aristizabal, C.; Ryu, H.; Edmonds, M. T.; Tsai, H.-Z.; Riss, A.; Mo, S.-K.; Lee, D.; Zettl, A.; Hussain, Z.; Shen, Z.-X.; Crommie, M. F. Characterization of Collective Ground States in Single-Layer NbSe_2 . *Nat. Phys.* **2016**, *12* (1), 92–97.
<https://doi.org/10.1038/nphys3527>.
- (6) Vaño, V.; Amini, M.; Ganguli, S. C.; Chen, G.; Lado, J. L.; Kezilebieke, S.; Liljeroth, P. Artificial Heavy Fermions in a van Der Waals Heterostructure. *Nature* **2021**, *599* (7886), 582–586. <https://doi.org/10.1038/s41586-021-04021-0>.
- (7) Chen, P.; Chan, Y.-H.; Fang, X.-Y.; Zhang, Y.; Chou, M. Y.; Mo, S.-K.; Hussain, Z.; Fedorov, A.-V.; Chiang, T.-C. Charge Density Wave Transition in Single-Layer Titanium Diselenide. *Nat. Commun.* **2015**, *6* (1), 8943.
<https://doi.org/10.1038/ncomms9943>.
- (8) Feng, J.; Biswas, D.; Rajan, A.; Watson, M. D.; Mazzola, F.; Clark, O. J.; Underwood, K.; Marković, I.; McLaren, M.; Hunter, A.; Burn, D. M.; Duffy, L. B.; Barua, S.; Balakrishnan, G.; Bertran, F.; Le Fèvre, P.; Kim, T. K.; van der Laan, G.; Hesjedal, T.; Wahl, P.; King, P. D. C. Electronic Structure and Enhanced Charge-Density Wave Order of Monolayer VSe_2 . *Nano Lett.* **2018**, *18* (7), 4493–4499.
<https://doi.org/10.1021/acs.nanolett.8b01649>.
- (9) Duvjir, G.; Choi, B. K.; Jang, I.; Ulstrup, S.; Kang, S.; Thi Ly, T.; Kim, S.; Choi, Y. H.; Jozwiak, C.; Bostwick, A.; Rotenberg, E.; Park, J.-G.; Sankar, R.; Kim, K.-S.; Kim, J.; Chang, Y. J. Emergence of a Metal–Insulator Transition and High-Temperature Charge-Density Waves in VSe_2 at the Monolayer Limit. *Nano Lett.* **2018**, *18* (9), 5432–5438.
<https://doi.org/10.1021/acs.nanolett.8b01764>.
- (10) O’Hara, D. J.; Zhu, T.; Trout, A. H.; Ahmed, A. S.; Luo, Y. K.; Lee, C. H.; Brenner, M. R.; Rajan, S.; Gupta, J. A.; McComb, D. W.; Kawakami, R. K. Room Temperature Intrinsic Ferromagnetism in Epitaxial Manganese Selenide Films in the Monolayer Limit. *Nano Lett.* **2018**, *18* (5), 3125–3131.
<https://doi.org/10.1021/acs.nanolett.8b00683>.
- (11) Zhang, X.; Lu, Q.; Liu, W.; Niu, W.; Sun, J.; Cook, J.; Vaninger, M.; Miceli, P. F.; Singh, D. J.; Lian, S.-W.; Chang, T.-R.; He, X.; Du, J.; He, L.; Zhang, R.; Bian, G.; Xu, Y. Room-Temperature Intrinsic Ferromagnetism in Epitaxial CrTe_2 Ultrathin Films. *Nat. Commun.* **2021**, *12* (1), 2492. <https://doi.org/10.1038/s41467-021-22777-x>.

- 1
2
3
4
5
6
7
8
9
10
11
12
13
14
15
16
17
18
19
20
21
22
23
24
25
26
27
28
29
30
31
32
33
34
35
36
37
38
39
40
41
42
43
44
45
46
47
48
49
50
51
52
53
54
55
56
57
58
59
60
- (12) Nakata, Y.; Sugawara, K.; Shimizu, R.; Okada, Y.; Han, P.; Hitosugi, T.; Ueno, K.; Sato, T.; Takahashi, T. Monolayer 1T-NbSe₂ as a Mott Insulator. *NPG Asia Mater.* **2016**, *8* (11), e321–e321. <https://doi.org/10.1038/am.2016.157>.
 - (13) Chen, Y.; Ruan, W.; Wu, M.; Tang, S.; Ryu, H.; Tsai, H.-Z.; Lee, R.; Kahn, S.; Liou, F.; Jia, C.; Albertini, O. R.; Xiong, H.; Jia, T.; Liu, Z.; Sobota, J. A.; Liu, A. Y.; Moore, J. E.; Shen, Z.-X.; Louie, S. G.; Mo, S.-K.; Crommie, M. F. Strong Correlations and Orbital Texture in Single-Layer 1T-TaSe₂. *Nat. Phys.* **2020**, *16*, 218–224. <https://doi.org/10.1038/s41567-019-0744-9>.
 - (14) Song, S.; Keum, D. H.; Cho, S.; Perello, D.; Kim, Y.; Lee, Y. H. Room Temperature Semiconductor–Metal Transition of MoTe₂ Thin Films Engineered by Strain. *Nano Lett.* **2016**, *16* (1), 188–193. <https://doi.org/10.1021/acs.nanolett.5b03481>.
 - (15) Wang, Y.; Xiao, J.; Zhu, H.; Li, Y.; Alsaied, Y.; Fong, K. Y.; Zhou, Y.; Wang, S.; Shi, W.; Wang, Y.; Zettl, A.; Reed, E. J.; Zhang, X. Structural Phase Transition in Monolayer MoTe₂ Driven by Electrostatic Doping. *Nature* **2017**, *550* (7677), 487–491. <https://doi.org/10.1038/nature24043>.
 - (16) Zhu, X.; Li, D.; Liang, X.; Lu, W. D. Ionic Modulation and Ionic Coupling Effects in MoS₂ Devices for Neuromorphic Computing. *Nat. Mater.* **2019**, *18* (2), 141–148. <https://doi.org/10.1038/s41563-018-0248-5>.
 - (17) Maximenko, Y.; Chang, Y.; Chen, G.; Hirsbrunner, M. R.; Swiech, W.; Hughes, T. L.; Wagner, L. K.; Madhavan, V. Nanoscale Studies of Electric Field Effects on Monolayer 1T'-WTe₂. *Npj Quantum Mater.* **2022**, *7* (1), 1–6. <https://doi.org/10.1038/s41535-022-00433-x>.
 - (18) Zhu, T.; Ruan, W.; Wang, Y.-Q.; Tsai, H.-Z.; Wang, S.; Zhang, C.; Wang, T.; Liou, F.; Watanabe, K.; Taniguchi, T.; Neaton, J. B.; Weber-Bargioni, A.; Zettl, A.; Qiu, Z. Q.; Zhang, G.; Wang, F.; Moore, J. E.; Crommie, M. F. Imaging Gate-Tunable Tomonaga–Luttinger Liquids in 1H-MoSe₂ Mirror Twin Boundaries. *Nat. Mater.* **2022**, *21* (7), 748–753. <https://doi.org/10.1038/s41563-022-01277-3>.
 - (19) Duerloo, K.-A. N.; Li, Y.; Reed, E. J. Structural Phase Transitions in Two-Dimensional Mo- and W-Dichalcogenide Monolayers. *Nat. Commun.* **2014**, *5* (1), 4214. <https://doi.org/10.1038/ncomms5214>.
 - (20) Li, Y.; Duerloo, K.-A. N.; Wauson, K.; Reed, E. J. Structural Semiconductor-to-Semimetal Phase Transition in Two-Dimensional Materials Induced by Electrostatic Gating. *Nat. Commun.* **2016**, *7* (1), 10671. <https://doi.org/10.1038/ncomms10671>.
 - (21) Zhang, J.; Liu, J.; Huang, J. L.; Kim, P.; Lieber, C. M. Creation of Nanocrystals Through a Solid-Solid Phase Transition Induced by an STM Tip. *Science* **1996**, *274* (5288), 757–760. <https://doi.org/10.1126/science.274.5288.757>.
 - (22) Kim, J.-J.; Park, C.; Yamaguchi, W.; Shiino, O.; Kitazawa, K.; Hasegawa, T. Observation of a Phase Transition from the T Phase to the H Phase Induced by a STM Tip in 1T-TaS₂. *Phys. Rev. B* **1997**, *56* (24), R15573–R15576. <https://doi.org/10.1103/PhysRevB.56.R15573>.
 - (23) Bischoff, F.; Auwärter, W.; Barth, J. V.; Schiffrin, A.; Fuhrer, M.; Weber, B. Nanoscale Phase Engineering of Niobium Diselenide. *Chem. Mater.* **2017**, *29* (23), 9907–9914. <https://doi.org/10.1021/acs.chemmater.7b03061>.
 - (24) Zhang, F.; Wang, Z.; Dong, J.; Nie, A.; Xiang, J.; Zhu, W.; Liu, Z.; Tao, C. Atomic-Scale Observation of Reversible Thermally Driven Phase Transformation in 2D In₂Se₃. *ACS Nano* **2019**, *13* (7), 8004–8011. <https://doi.org/10.1021/acsnano.9b02764>.
 - (25) Cho, S.; Kim, S.; Kim, J. H.; Zhao, J.; Seok, J.; Keum, D. H.; Baik, J.; Choe, D.-H.; Chang, K. J.; Suenaga, K.; Kim, S. W.; Lee, Y. H.; Yang, H. Phase Patterning for Ohmic Homo Junction Contact in MoTe₂. *Science* **2015**, *349* (6248), 625–628. <https://doi.org/10.1126/science.aab3175>.

- 1
2
3
4
5
6
7
8
9
10
11
12
13
14
15
16
17
18
19
20
21
22
23
24
25
26
27
28
29
30
31
32
33
34
35
36
37
38
39
40
41
42
43
44
45
46
47
48
49
50
51
52
53
54
55
56
57
58
59
60
- (26) Pedramrazi, Z.; Herbig, C.; Pulkin, A.; Tang, S.; Phillips, M.; Wong, D.; Ryu, H.; Pizzochero, M.; Chen, Y.; Wang, F.; Mele, E. J.; Shen, Z.-X.; Mo, S.-K.; Yazyev, O. V.; Crommie, M. F. Manipulating Topological Domain Boundaries in the Single-Layer Quantum Spin Hall Insulator 1T'-WSe₂. *Nano Lett.* **2019**, *19*, 5634–5639. <https://doi.org/10.1021/acs.nanolett.9b02157>.
- (27) Song, C.-L.; Wang, Y.-L.; Jiang, Y.-P.; Li, Z.; Wang, L.; He, K.; Chen, X.; Ma, X.-C.; Xue, Q.-K. Molecular-Beam Epitaxy and Robust Superconductivity of Stoichiometric FeSe Crystalline Films on Bilayer Graphene. *Phys. Rev. B* **2011**, *84* (2), 020503. <https://doi.org/10.1103/PhysRevB.84.020503>.
- (28) Lee, J.; Wong, D.; Velasco Jr, J.; Rodriguez-Nieva, J. F.; Kahn, S.; Tsai, H.-Z.; Taniguchi, T.; Watanabe, K.; Zettl, A.; Wang, F.; Levitov, L. S.; Crommie, M. F. Imaging Electrostatically Confined Dirac Fermions in Graphene Quantum Dots. *Nat. Phys.* **2016**, *12* (11), 1032–1036. <https://doi.org/10.1038/nphys3805>.
- (29) Chang, K.; Küster, F.; Miller, B. J.; Ji, J.-R.; Zhang, J.-L.; Sessi, P.; Barraza-Lopez, S.; Parkin, S. S. P. Microscopic Manipulation of Ferroelectric Domains in SnSe Monolayers at Room Temperature. *Nano Lett.* **2020**, *20* (9), 6590–6597. <https://doi.org/10.1021/acs.nanolett.0c02357>.
- (30) Perdew, J. P.; Ruzsinszky, A.; Csonka, G. I.; Vydrov, O. A.; Scuseria, G. E.; Constantin, L. A.; Zhou, X.; Burke, K. Restoring the Density-Gradient Expansion for Exchange in Solids and Surfaces. *Phys. Rev. Lett.* **2008**, *100* (13), 136406. <https://doi.org/10.1103/PhysRevLett.100.136406>.
- (31) Winiarski, M. J.; Samsel-Czekala, M.; Ciechan, A. Strain Effects on the Electronic Structure of the Iron Selenide Superconductor. *EPL Europhys. Lett.* **2012**, *100* (4), 47005. <https://doi.org/10.1209/0295-5075/100/47005>.
- (32) Zhang, G.-X.; Reilly, A. M.; Tkatchenko, A.; Scheffler, M. Performance of Various Density-Functional Approximations for Cohesive Properties of 64 Bulk Solids. *New J. Phys.* **2018**, *20* (6), 063020. <https://doi.org/10.1088/1367-2630/aac7f0>.
- (33) Li, T.; Zhang, X.; Zeng, Z. Factors Affecting the Electron–Phonon Coupling in FeSe under Pressure. *Phys. Chem. Chem. Phys.* **2021**, *23* (44), 25107–25113. <https://doi.org/10.1039/D1CP02749B>.
- (34) Liu, H.; Xue, Y. Van Der Waals Epitaxial Growth and Phase Transition of Layered FeSe₂ Nanocrystals. *Adv. Mater.* **2021**, *33* (17), 2008456. <https://doi.org/10.1002/adma.202008456>.
- (35) Kresse, G.; Furthmüller, J. Efficient Iterative Schemes for Ab Initio Total-Energy Calculations Using a Plane-Wave Basis Set. *Phys. Rev. B* **1996**, *54* (16), 11169–11186. <https://doi.org/10.1103/PhysRevB.54.11169>.
- (36) Kresse, G.; Joubert, D. From ultrasoft pseudopotentials to the projector augmented-wave method. *Phys. Rev. B* **1999**, *59* (3), 1758–1775. <https://doi.org/10.1103/PhysRevB.59.1758>.
- (37) Berland, K.; Cooper, V. R.; Lee, K.; Schröder, E.; Thonhauser, T.; Hyldgaard, P.; Lundqvist, B. I. Van Der Waals Forces in Density Functional Theory: A Review of the vdW-DF Method. *Rep. Prog. Phys.* **2015**, *78* (6), 066501. <https://doi.org/10.1088/0034-4885/78/6/066501>.
- (38) Klimeš, J.; Bowler, D. R.; Michaelides, A. Chemical Accuracy for the van Der Waals Density Functional. *J. Phys. Condens. Matter* **2009**, *22* (2), 022201. <https://doi.org/10.1088/0953-8984/22/2/022201>.
- (39) Lee, K.; Murray, É. D.; Kong, L.; Lundqvist, B. I.; Langreth, D. C. Higher-Accuracy van Der Waals Density Functional. *Phys. Rev. B* **2010**, *82* (8), 081101. <https://doi.org/10.1103/PhysRevB.82.081101>.

- 1
2
3 (40) Klimeš, J.; Bowler, D. R.; Michaelides, A. Van Der Waals Density Functionals Applied
4 to Solids. *Phys. Rev. B* **2011**, *83* (19), 195131.
5 <https://doi.org/10.1103/PhysRevB.83.195131>.
6
7 (41) Anisimov, V. I.; Gunnarsson, O. Density-Functional Calculation of Effective Coulomb
8 Interactions in Metals. *Phys. Rev. B* **1991**, *43* (10), 7570–7574.
9 <https://doi.org/10.1103/PhysRevB.43.7570>.
10
11 (42) Anisimov, V. I.; Zaanen, J.; Andersen, O. K. Band Theory and Mott Insulators: Hubbard
12 U Instead of Stoner I. *Phys. Rev. B* **1991**, *44* (3), 943–954.
13 <https://doi.org/10.1103/PhysRevB.44.943>.
14
15 (43) Dudarev, S. L.; Botton, G. A.; Savrasov, S. Y.; Humphreys, C. J.; Sutton, A. P.
16 Electron-Energy-Loss Spectra and the Structural Stability of Nickel Oxide: An
17 LSDA+U Study. *Phys. Rev. B* **1998**, *57* (3), 1505–1509.
18 <https://doi.org/10.1103/PhysRevB.57.1505>.
19
20
21
22
23
24
25
26
27
28
29
30
31
32
33
34
35
36
37
38
39
40
41
42
43
44
45
46
47
48
49
50
51
52
53
54
55
56
57
58
59
60

Figures

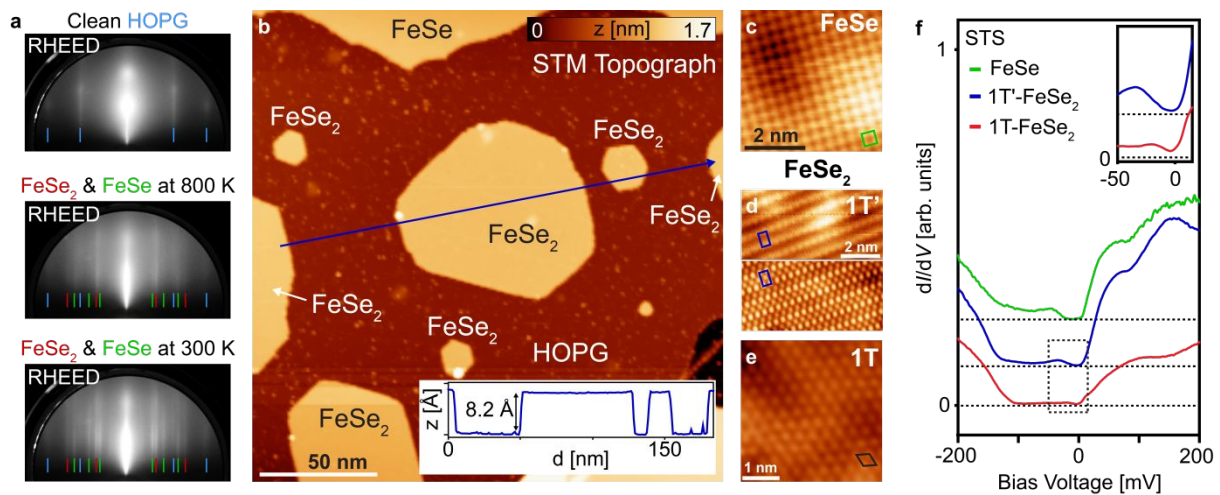


Figure 1 | Growth and structural characterization of FeSe₂ monolayers.

(a) RHEED patterns (top to bottom) of clean HOPG (blue), a mixture of monolayer FeSe₂ (red) and monolayer FeSe (green) after growth at 800 K, and after cooling down to 300 K. (b) Large-scale STM image of typical MBE-grown sample ($V_B = -1.0$ V, $I_T = 10$ pA). The inset shows the height profile along the blue line. (c) Close-up STM image of an FeSe monolayer with square unit cell (green) ($V_B = -1.0$ V, $I_T = 100$ pA). (d) Close-up STM image of monolayer 1T'-FeSe₂ with rectangular unit cell (blue) (top: $V_B = -1.0$ V, $I_T = 10$ pA, bottom: $V_B = -1.0$ V, $I_T = 100$ pA). (e) Close-up STM image of 1T-FeSe₂ monolayer with hexagonal unit cell (black) ($V_B = -0.3$ V, $I_T = 100$ pA). (f) STS spectra of monolayer FeSe (green), 1T'-FeSe₂ (blue), and 1T-FeSe₂ (red) (lock-in $V_{mod} = 2$ mV). The curves have been shifted vertically for easier viewing (dashed lines show $dI/dV = 0$ for each curve). Inset shows STS spectra in low-bias range for monolayer 1T'-FeSe₂ (blue) and 1T-FeSe₂ (red) (lock-in $V_{mod} = 2$ mV). Tip stabilization setpoint for STS: $V_B = -0.2$ V, $I_T = 100$ pA.

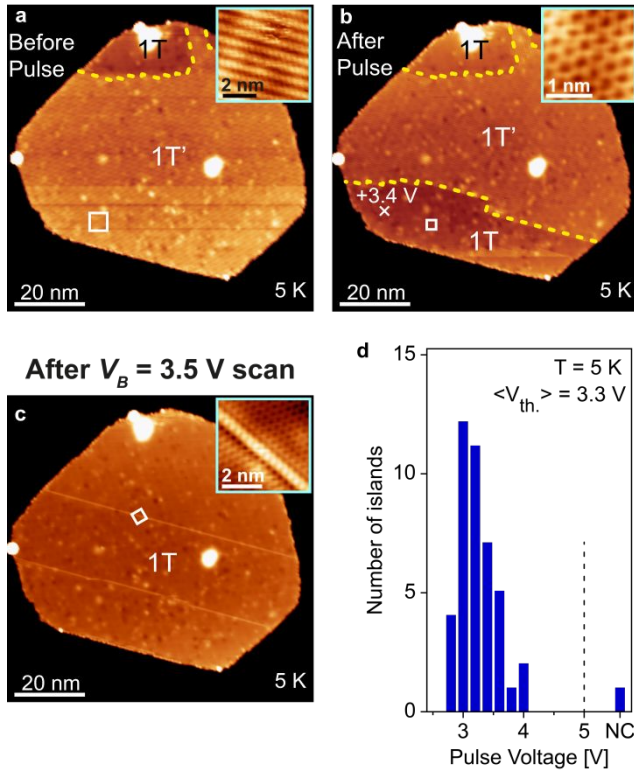


Figure 2 | Electrically-induced structural phase transition in FeSe₂ monolayers.

(a) STM image of stripe phase FeSe₂ monolayer island before any STM tip manipulation ($V_B = -1.0$ V, $I_T = 10$ pA). The boundary between the 1T' stripe phase and the 1T hexagonal phase of the FeSe₂ monolayer is indicated by a yellow dashed line. Inset shows a close-up image of the stripe phase ($V_B = -1.0$ V, $I_T = 10$ pA). (b) Same island shown in (a) after a +3.4 V voltage pulse applied at the position indicated by the white "x". Inset shows a close-up image of the hexagonal 1T phase ($V_B = -1.0$ V, $I_T = 10$ pA). (c) The same island after STM scanning with $V_B = +3.5$ V and $I_T = 10$ pA. Inset shows a close-up image of the newly converted 1T hexagonal phase ($V_B = -0.3$ V, $I_T = 100$ pA). (d) Histogram shows the number of islands converted from stripe phase to hexagonal phase and the minimum voltage pulse required for each conversion. Islands that did not exhibit a phase change from stripe to hexagonal phase for pulses up to 5 V are counted as "non-convertible" (NC).

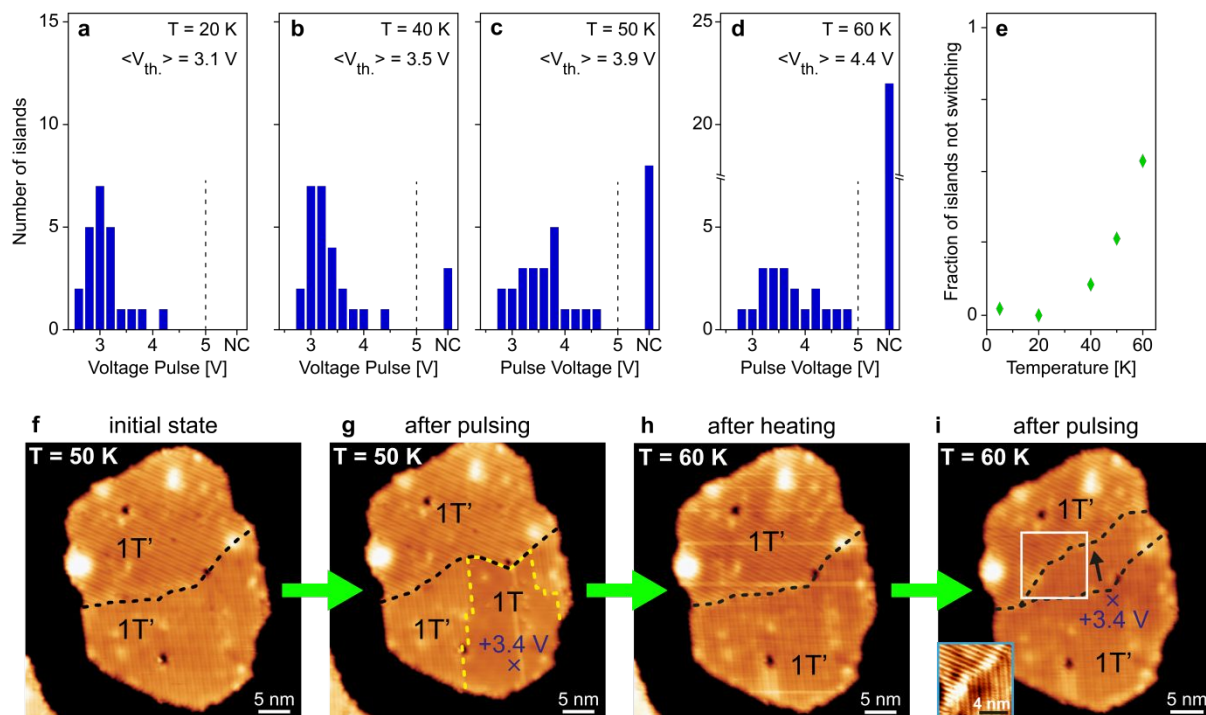


Figure 3 | Thermal reversibility of the structural phase transition in FeSe₂ monolayers.

Histograms show the number of monolayer islands converted from stripe phase to hexagonal phase (i.e., 1T' to 1T phase) and the minimum voltage pulse required for conversion at (a) $T = 20\text{ K}$, (b) $T = 40\text{ K}$, (c) $T = 50\text{ K}$, and (d) $T = 60\text{ K}$. Islands not undergoing phase conversion for pulses up to 5 V are counted as “non-convertible” (NC). (e) The temperature dependence of the total fraction of islands counted as non-convertible. STM images of the same monolayer FeSe₂ island (f) before and (g) after a +3.4 V pulse at the position indicated by the blue “x”. (h) The same island after increasing the sample temperature to 60 K. (i) The same island after applying a +3.4 V pulse at the position depicted by the blue “x” ($T = 60\text{ K}$). The boundary between two rotated stripe domains shifts after the voltage pulse as shown by the dashed black lines.

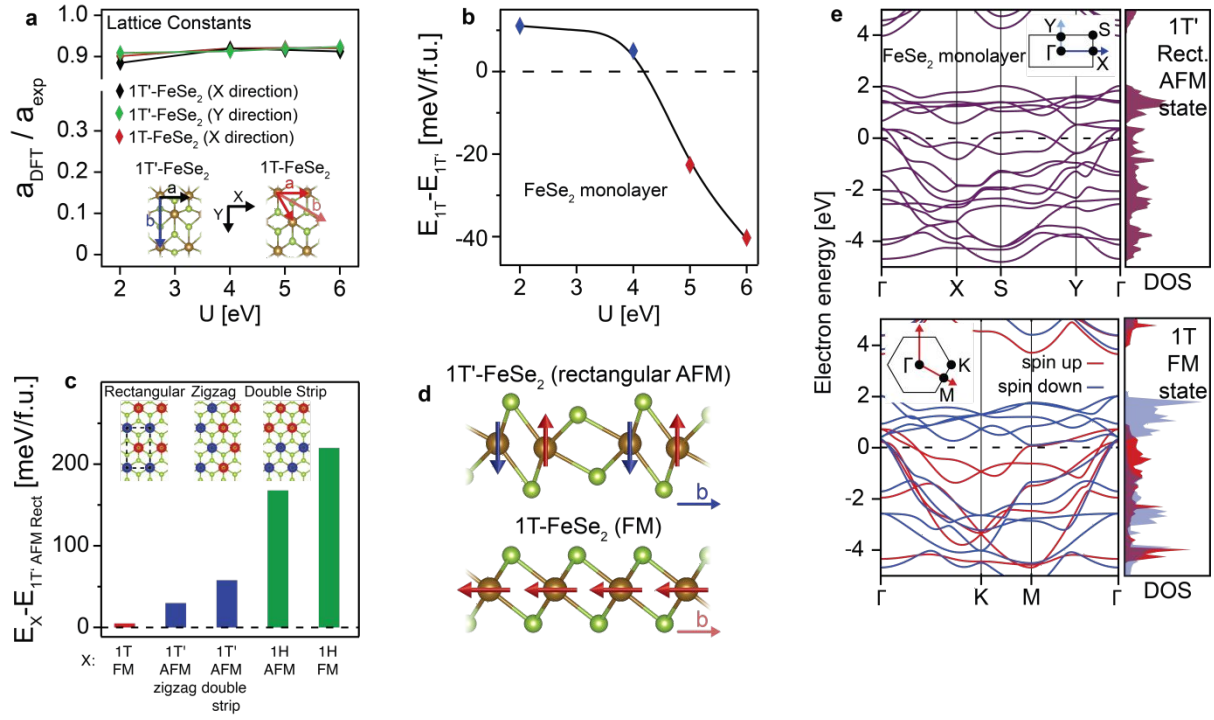


Figure 4 | Calculated energetics of FeSe₂ monolayers.

(a) Lattice constants of monolayer 1T'-FeSe₂ along X direction (black), monolayer 1T'-FeSe₂ along Y direction (green), and monolayer 1T-FeSe₂ along X direction (red) derived from DFT+U calculations for different values of U (normalized to the corresponding experimental lattice constants). **(b)** Total energy difference between the monolayer 1T- and 1T'-FeSe₂ structures as a function of the Hubbard parameter U in DFT+U calculations. **(c)** Total energy difference between monolayer 1T'-FeSe₂ with a rectangular antiferromagnetic (AFM) configuration and different X-FeSe₂ polymorphs where X = {1T', 1T, 1H} exhibiting different magnetic ground states (U = 4 eV). The inset shows the three possible calculated 1T' AFM configurations (red means spin up and blue means spin down). **(d)** Magnetic ordering for monolayer 1T'-FeSe₂ in the rectangular AFM state and monolayer 1T-FeSe₂ in the FM state along the b-direction as defined in **(a)** (the distorted 1T' structure is exaggerated for clarity). **(e)** Band structure and density of states for rectangular AFM monolayer 1T'-FeSe₂ (top) and FM monolayer 1T-FeSe₂ (bottom).